

Balmer and Paschen jump temperature determinations in low-metallicity emission-line galaxies

Natalia G. Guseva

Main Astronomical Observatory, National Academy of Sciences of Ukraine, 03680, Kyiv, Ukraine

`guseva@mao.kiev.ua`

Yuri I. Izotov

Main Astronomical Observatory, National Academy of Sciences of Ukraine, 03680, Kyiv, Ukraine

`izotov@mao.kiev.ua`

and

Trinh X. Thuan

Astronomy Department, University of Virginia, Charlottesville, VA 22903

`txt@virginia.edu`

ABSTRACT

We have used the Balmer and Paschen jumps to determine the temperatures of the H^+ zones of a total sample of 47 H II regions. The Balmer jump was used on MMT spectrophotometric data of 22 low-metallicity H II regions in 18 blue compact dwarf (BCD) galaxies and of one H II region in the spiral galaxy M101. The Paschen jump was used on spectra of 24 H II emission-line galaxies selected from the Data Release 3 of the Sloan Digital Sky Survey (SDSS). To derive the temperatures, we have used a Monte Carlo technique varying the electron temperature in the H^+ zone, the extinction of the ionized gas and that of the stellar population, the relative contribution of the ionized gas to the total emission and the star formation history to fit the spectral energy distribution of the galaxies. For the MMT spectra, the fit was done in the wavelength range of 3200 – 5200Å which includes the Balmer discontinuity, and for the SDSS spectra, in the wavelength range of 3900 – 9200Å which includes the Paschen discontinuity. We find for our sample of H II regions that the temperatures of the O^{2+} zones determined from the nebular to auroral line intensity ratio of doubly ionized oxygen $[O III] \lambda(4959+5007)/\lambda 4363$ do not differ, in a statistical sense, from the temperatures of the H^+ zones determined from fitting the Balmer and Paschen jumps and the SEDs. We cannot rule out small temperature differences of the order of 3–5%.

Subject headings: galaxies: irregular — galaxies: starburst — galaxies: ISM — galaxies: abundances

arXiv:astro-ph/0603134v1 6 Mar 2006

1. Introduction

The knowledge of the temperature structure of an H II region is essential for the determination of its element abundances. Heavy element abundances are typically derived from fluxes of collisionally excited forbidden lines in the optical range and they depend very sensitively (exponentially) on the adopted electron temperature. Since different ions reside in different parts of the H II region with different electron temperatures, an appropriately determined temperature is required for each ionic species to correctly derive its abundance. Fluxes of the recombination lines of hydrogen, helium and some heavy elements seen in the optical spectra of H II regions are less sensitive to electron temperature. However for some scientific problems, a very high precision in the element abundances derived from recombination lines is required. For example, the helium primordial abundance needs to be determined to better than about 1-2% to yield interesting cosmological constraints. In those cases, to reach the desired precision, the variations of the electron temperature in the H II region need to be taken into account for the recombination transitions as well.

There are several known methods for the determination of the electron temperature T_e in H II regions. One of them is based on the temperature-sensitive intensity ratios of collisionally excited forbidden lines of different ions, such as [O III] $\lambda(4959+5007)/\lambda 4363$, [Ne III] $\lambda 3868/\lambda 3342$, [Ar III] $\lambda 7135/\lambda 5192$, [N II] $\lambda(6548+6584)/\lambda 5754$, [O II] $\lambda(7320+7330)/\lambda 3727$ and others (Aller 1984). Most often, it is the nebular to auroral line intensity ratio of doubly ionized oxygen [O III] $\lambda(4959+5007)/\lambda 4363$ that is used. Such a method can be applied to H II regions with $T_e \gtrsim 10^4 \text{K}$ where the auroral emission line [O III] $\lambda 4363$ is sufficiently bright to be detected (e.g. Izotov et al. 2006).

Another way for determining electron temperatures in H II regions relies on discontinuities in the continuum emission of hydrogen and helium free-bound recombination processes. Most often the Balmer discontinuity at 3646 Å and the Paschen discontinuity at 8207 Å are used. Peimbert (1967) was the first to use the Balmer discontinuity, or Balmer jump, to derive electron temperatures $T_e(\text{H}^+)$ in several Galactic H II regions, using the intensity ratio $\text{BJ}/I(\text{H}\beta)$, where $\text{BJ} = I(3646^-) - I(3646^+)$ is the value of the Balmer jump. Much later, to reduce the interstellar reddening effect on the determination of T_e , Liu et al. (2000) and Luo et al. (2001) have proposed to use the H11 hydrogen emission line instead of the H β emission line, defining the Balmer jump as $\text{BJ}/\text{H11} = [I_c(\lambda 3646) - I_c(\lambda 3681)]/I(\text{H11 } \lambda 3770)$. More recently, Zhang et al. (2004) have suggested a new approach to derive the electron temperature and density in H II regions from the observed nebular hydrogen recombination spectrum. The method is based on fitting the dereddened observed spectrum around the region of the Balmer jump with model spectra calculated from recombination theory by varying the electron temperature and density.

While these methods of electron temperature determination may in principle be applied to any type of photoionized gaseous region, in practice they have been mainly applied to planetary nebulae (PNe) (e.g. Liu et al. 2000; Luo et al. 2001; Ruiz et al. 2003; Zhang et al. 2004; Peimbert et al. 2004; Wesson et al. 2005). Only a few electron temperature measurements from

the Balmer jump or Paschen jump techniques exist in the literature for H II regions in the Milky Way and several nearby galaxies (e.g. Peimbert & Torres-Peimbert 1992; Peimbert et al. 1993, 2000; Peimbert 2003; Esteban et al. 1998; García-Rojas et al. 2004, 2005, 2006). For example, González-Delgado et al. (1994) have used the Paschen jump to derive the electron temperature from the hydrogen recombination spectrum in two H II regions of the low-metallicity ($Z \sim Z_{\odot}/10$) blue compact dwarf (BCD) galaxy NGC 2366.

A general finding of the above work for PNe is that the electron temperature $T_e(\text{H}^+)$ derived from the Balmer jump is systematically lower than the temperature $T_e(\text{O III})$ derived from the collisionally excited [O III] emission lines. Furthermore, Zhang et al. (2005a,b) by using the He I recombination lines and the He I discontinuity at 3421Å to measure electron temperatures, have found that $T_e(\text{He}^+)$ in PNe is significantly lower than $T_e(\text{H}^+)$. As for H II regions, the situation is not so clear. In some H II regions the electron temperature $T_e(\text{H}^+)$ is appreciably lower than $T_e(\text{O III})$ (e.g., in M17, Peimbert & Torres-Peimbert 1992; Peimbert et al. 1993) while in some other H II regions, the two temperatures are comparable (e.g., in Orion nebula, Esteban et al. 1998).

The exact cause of these temperature differences is still unclear. Following Peimbert (1967), they are usually attributed to temperature fluctuations in chemically homogeneous gaseous nebulae. However, no homogeneous photoionization models can give temperature fluctuations as large as those observed. If we characterize the spatial temperature fluctuations in H II regions by t^2 , the mean square temperature variation (Peimbert 1967), then models give t^2 in the 0.002 – 0.025 range, with typical values around 0.005, while observations give t^2 in the 0.02 – 0.04 range (see the review in O’Dell et al. 2003). To reduce the discrepancy between models and observations, Viegas & Clegg (1994) have proposed that chemically homogeneous nebulae contain condensations with both temperature and density variations. However, Liu et al. (2001) have concluded that temperature fluctuations alone are unable to explain the large differences between $T_e(\text{H}^+)$ and $T_e(\text{O III})$ in PNe. Instead, they proposed that PNe contain H-deficient clumps with temperatures, densities and chemical compositions different from those of the diffuse ionized gas around the clumps. On the other hand, O’Dell et al. (2003) have studied small-scale temperature fluctuations in the Orion nebula with *HST* images, but did not find statistically significant variations of the columnar electron temperatures with distance from the ionizing star, in agreement with photoionization models for chemically homogeneous gaseous nebulae of constant density. However, small-scale variations (over a few arcsec or ~ 0.005 pc) were found. Those authors concluded that none of the physical mechanisms that have been proposed thus far is able to account for the observed temperature differences.

The difference between $T_e(\text{H}^+)$ and $T_e(\text{O III})$ may have important consequences for the heavy element abundance determination in H II regions, as their derived abundances depend sensitively on the adopted temperature. Indeed, in the majority of such studies (e.g. Izotov et al. 2006), the heavy element abundances are derived assuming that the temperature of the H^+ zone is equal to the temperature of the O^{2+} zone. If instead, $T_e(\text{H}^+)$ is smaller than $T_e(\text{O III})$, then the heavy element abundances would be increased. This issue is especially important for the determination

of the primordial He abundance from spectra of low-metallicity BCDs. In this work (Izotov et al. 1994, 1997; Izotov & Thuan 1998; Olive et al. 1997; Olive & Skillman 2004; Izotov & Thuan 2004), it is assumed that $T_e(\text{H}^+) = T_e(\text{O III})$. If indeed $T_e(\text{H}^+)$ is less than $T_e(\text{O III})$ in the H II regions of the low-metallicity BCDs, then the derived He abundances would be lower, resulting in a lower primordial He abundance (Luridiana et al. 2003).

In all the above studies, direct measurements of $T_e(\text{H}^+)$ by the Balmer or Paschen jump techniques have been carried out only for relatively high-metallicity H II regions. The metallicity range is generally between 1/3 solar and solar metallicity. With the exception of Mrk 71 = NGC 2363 (González-Delgado et al. 1994) with a metallicity of 1/10 that of the Sun, no direct measurements of $T_e(\text{H}^+)$ in very low-metallicity BCDs have been done. Yet, those very metal-deficient objects which span a metallicity range of about 1/50 to 1/10 of the Sun’s metallicity are precisely those used in the determination of the primordial He abundance. Thus to assess a potential source of systematic error in the primordial He abundance measurement which may compromise the reliability of the cosmological constraints that are derived from it, it is crucial to investigate whether temperature differences are as important in low-metallicity BCDs as they are in high-metallicity H II regions and PNe.

We have thus embarked on an observational program with the MMT to obtain blue spectra of a large sample of BCDs in the 3200 – 5200Å wavelength range which includes the region of the Balmer jump. In addition, we have supplemented our data with spectra of bright H II regions from the Data Release 3 (DR3) of the Sloan Digital Sky Survey (SDSS) in the wavelength range 3800 – 9200Å, which includes the Paschen jump region. We wish to directly measure the electron temperature $T_e(\text{H}^+)$ in these H II regions by applying either the Balmer jump technique on the MMT spectra or the Paschen jump technique on the SDSS spectra. We present in this paper the first results of the program. In Section 2, we describe the observational sample and the method used to determine $T_e(\text{H}^+)$ in the H II regions. We compare $T_e(\text{H}^+)$ and $T_e(\text{O III})$ for our sample of H II regions and discuss the issue of temperature differences in low-metallicity emission-line galaxies in Section 3. We summarize our conclusions in Section 4.

2. Electron temperature determination with the Balmer and Paschen jumps

2.1. Observations and data reduction

The MMT observational sample consists of 22 low-metallicity H II regions in 18 BCDs and of one H II region, J1404+5423, in the spiral galaxy M101. The sample is the same as the one used by Thuan & Izotov (2005) to study high-ionization emission lines in low-metallicity BCDs. The selection criteria of the sample are given in Thuan & Izotov (2005), so we will not repeat them here in detail. For our present purposes, it is sufficient to know that the BCDs were chosen to span a large metallicity range, from about 1/60 of solar metallicity for SBS 0335–052W to about 1/3 of solar metallicity for Mrk 35 = Haro 3, so we can study any trend of differences between

$T_e(\text{H}^+)$ and $T_e(\text{O III})$ with metallicity. Since the electron temperature of an H II region depends on its metallicity, this ensures that the H II regions in our BCD sample span a large range of electron temperatures. They were also selected to cover a large range of equivalent widths of the H β emission line, with EW(H β) varying from 18Å to 397Å. Since EW(H β) is a measure of the relative contribution of the ionized gas emission to the total light, this allows to study how stellar emission affects the derived electron temperatures. The observed BCDs are listed in order of decreasing EW(H β), i.e. in order of increasing contribution of the stellar component to the total light, in Table 1. The general characteristics for each BCD can be found in Table 1 of Thuan & Izotov (2005). We can also determine electron temperatures from the Paschen jump at 8207 Å. To this end, we have extracted spectra of 24 bright H II regions from the DR3 of the SDSS which cover the red wavelength region and include the Paschen jump, and which constitute what will be designated hereafter as the SDSS sample. The SDSS sample includes eleven H II regions in dwarf emission-line galaxies, and 13 H II regions in spiral galaxies in a metallicity range from about 1/50 of solar metallicity for I Zw 18 SE to about 1/2 of solar metallicity for J1402+5416. The extracted H II regions with their derived parameters and spectroscopic SDSS ID numbers are listed in order of decreasing EW(H β) in Table 2. While the metallicity range of the SDSS sample is about the same as that of the MMT sample, the SDSS sample contains a larger fraction of high-metallicity H II regions.

The observations of the MMT sample were carried out with the 6.5-m MMT¹ on the nights of 2004 February 19–20 and 2005 February 4, using the Blue Channel of the MMT spectrograph. We used a 2'' \times 300'' slit and a 800 grooves/mm grating in first order. The above instrumental set-up gave a spatial scale along the slit of 0''.6 pixel⁻¹, a scale perpendicular to the slit of 0.75Å pixel⁻¹, a spectral range of 3200 – 5200Å and a spectral resolution of ~ 3 Å (FWHM). The seeing was in the range 1''–2''. The spectra of the majority of the galaxies have been obtained with the slit oriented with the parallactic angle. The only exceptions concern SBS 0335–052W and SBS 0335–052E where the slit was oriented along the major axes of the galaxies, with position angles of -30° and -80° respectively, and Mrk 71, where the slit was oriented along the position angle of $+60^\circ$, so as to go through the three brightest H II regions. In those cases, differential refraction may play a role, and we analyze its possible effect in Section 3. Three Kitt Peak IRS spectroscopic standard stars, G191B2B, Feige 34 and HZ 44 were observed at the beginning, middle and end of each night for flux calibration. For the final calibration curve, we adopt the mean of three derived response curves, which does not deviate by more than 1% from the response curves obtained from each standard star individually, over the whole wavelength range. Spectra of He-Ar comparison arcs were obtained before and after each observation to calibrate the wavelength scale. The log of observations is given in Table 2 of Thuan & Izotov (2005) and details of the data reduction can be found in the same paper.

¹The observations reported here were obtained at the MMT Observatory, a joint facility of the Smithsonian Institution and the University of Arizona.

For the present analysis, we have used the same one-dimensional spectra as those of Thuan & Izotov (2005). They have been extracted from the two-dimensional spectra using a $6'' \times 2''$ extraction aperture so as to cover the brightest parts of the H II regions. In the case of five BCDs, Mrk 71, I Zw 18, Mrk 35, Mrk 59 and Mrk 178, spectra of 2-3 different H II regions in the same galaxy have been extracted. In total, Thuan & Izotov (2005) extracted 27 one-dimensional spectra. However, since the spectra of I Zw 18C, Mrk 35 #2, Mrk 178 #2 and Mrk 178 #3 are too noisy for our present purposes (see their spectra in Fig. 2 of Thuan & Izotov 2005), we do not include them here.

The spectra for all 23 H II regions in the MMT sample are displayed in Figure 1. We have also shown a zoom of the Balmer jump region for four selected H II regions in Fig. 2. We show the spectra for the SDSS H II regions in Fig. 3. Since we are concerned with the Paschen jump region, we have displayed only the red part of each spectrum. All spectra have been reduced to zero redshift. The electron temperature $T_e(\text{O III})$, ionic and total element abundances of the H II regions in both the MMT and SDSS samples have been derived according to the prescriptions of Izotov et al. (2006). They are given in Thuan & Izotov (2005) for the H II regions in the MMT sample and in Izotov et al. (2006) for the SDSS sample. Relevant parameters such as the equivalent width $\text{EW}(\text{H}\beta)$, the oxygen abundance $12 + \log \text{O}/\text{H}$, and the extinction coefficient $C(\text{H}\beta)$ are given in Table 1 for the MMT objects and in Table 2 for the SDSS objects.

2.2. Monte Carlo calculations

The method consists of deriving the electron temperature $T_e(\text{H}^+)$ of H^+ zones by fitting a series of model spectral energy distributions (SEDs) to the observed ones and finding the best fits. The fit for each MMT spectrum is performed over the whole observed spectral range shortward of $\lambda 5200\text{\AA}$, which includes the Balmer jump region ($\lambda 3646\text{\AA}$). As for the SDSS sample, each fit is performed over a spectral range of $3900 - 9200\text{\AA}$, which includes the Paschen jump region ($\lambda 8207\text{\AA}$). Besides the electron temperature $T_e(\text{H}^+)$ which controls the magnitudes of the Balmer and Paschen jumps, the shape of the SED depends on several other parameters.

As each SED is the sum of both stellar and ionized gas emission, its shape depends on the relative contribution of these two components. In BCDs, the contribution of the ionized gas emission can be very large. However, the equivalent widths of the hydrogen emission lines never reach the theoretical values for pure gaseous emission, implying a non-zero contribution of stellar emission in all objects. The contribution of gaseous emission relative to stellar emission can be parametrized by the equivalent width of the $\text{H}\beta$ emission line $\text{EW}(\text{H}\beta)$. Given a temperature, the ratio of the gaseous emission to the total emission is equal to the ratio of the observed $\text{EW}(\text{H}\beta)$ to the equivalent width of $\text{H}\beta$ expected for pure gaseous emission. The shape of the spectrum depends also on reddening. The extinction coefficient for the ionized gas $C(\text{H}\beta)_{\text{gas}}$ can be obtained from the observed hydrogen Balmer decrement. However, there is no direct way to derive the extinction coefficient $C(\text{H}\beta)_{\text{stars}}$ for the stellar emission which can be different from the ionized gas extinction coefficient. Finally,

the SED depends on the star formation history of the galaxy.

We have carried out a series of Monte Carlo simulations to reproduce the SED in each H II region of our sample. To calculate the contribution of the stellar emission to the SEDs, we have adopted the grid of the Padua stellar evolution models by Girardi et al. (2000)² with heavy element mass fractions $Z = 0.0001, 0.0004, 0.001, 0.004, 0.008$. To check the sensitivity of our calculations to the particular stellar tracks adopted, we have also considered Geneva tracks (Lejeune & Schaerer 2001). With these tracks, we obtained results similar to those gotten with the Padua ones. Nevertheless, the Geneva models are less appropriate for our goals as they do not include stellar models older than 1 Gyr. Therefore we do not include the results obtained with the Geneva models in this paper. To reproduce the SED of the stellar component with any star formation history, we have calculated with the package PEGASE.2 (Fioc & Rocca-Volmerange 1997) a grid of instantaneous burst SEDs in a wide range of ages, from 0.5 Myr to 15 Gyr. We have adopted a stellar initial mass function with a Salpeter slope, an upper mass limit of $100 M_{\odot}$ and a lower mass limit of $0.1 M_{\odot}$. Then the SED with any star formation history can be obtained by integrating the instantaneous bursts SEDs over time with a specified time-varying star formation rate.

More than $\sim 90\%$ of the emission of an H II region is due to the ongoing burst of star formation. Therefore, the shape of its spectrum is not very sensitive to variations in the star formation history of the older stellar populations. Thus, as a first approximation, we have approximated the star formation history in each BCD by two short bursts with different strengths: a recent burst with age $t(\text{young}) < 10$ Myr which accounts for the young stellar population and a prior burst with age $t(\text{old})$ varying between 10 Myr and 15 Gyr and responsible for the older stars. The contribution of each burst to the SED is defined by the ratio of the masses of stellar populations formed respectively in the old and young bursts, $b = M(\text{old})/M(\text{young})$, which we vary between 0.01 and 100. To check the sensitivity of our calculations to the adopted star formation history, we have also considered the case where star formation is continuous for the old stellar population.

The contribution of the gaseous emission was scaled to the stellar emission using the ratio of the observed equivalent width of the $H\beta$ emission line to the equivalent width of $H\beta$ expected for pure gaseous emission. The continuous gaseous emission is taken from Aller (1984) and includes hydrogen and helium free-bound, free-free and two-photon emission. In our models it is always calculated with the electron temperature $T_e(\text{H}^+)$ of the H^+ zone and with the chemical composition derived from the H II region spectrum. The observed emission lines corrected for reddening and scaled using the absolute flux of the $H\beta$ emission line were added to the calculated gaseous continuum. The fraction of the gaseous continuum to the total light depends on the adopted electron temperature $T_e(\text{H}^+)$ in the H^+ zone, since $\text{EW}(H\beta)$ for pure gaseous emission decreases with increasing $T_e(\text{H}^+)$. Given that $T_e(\text{H}^+)$ is not necessarily equal to $T_e(\text{O III})$, we chose to vary it in the range $(0.7 - 1.3) \times T_e(\text{O III})$. Strong emission lines in BCDs (see Fig. 1) are usually measured with

²<http://pleiadi.pd.astro.it>.

good precision and so the equivalent width of the H β emission line and the extinction coefficient for the ionized gas are accurate to $\pm 5\%$ or $\pm 20\%$, respectively. Thus we vary EW(H β) between 0.95 and 1.05 times its nominal value. As for the extinction, we assume that the extinction $C(\text{H}\beta)_{stars}$ for the stellar light is the same as $C(\text{H}\beta)_{gas}$ for the ionized gas, and we vary both in the range $(0.8 - 1.2) \times C(\text{H}\beta)_{gas}$. We run a large number (either 10^5 or 10^6) of Monte Carlo models varying randomly $t(\text{young})$, $t(\text{old})$, b and $T_e(\text{H}^+)$ in a large range, and EW(H β), $C(\text{H}\beta)_{gas}$ and $C(\text{H}\beta)_{stars}$ in a relatively smaller range because the latter quantities are more directly constrained by observations. Because of the somewhat large number of parameters, the determination of $T_e(\text{H}^+)$ in any particular H II region may not be very certain. In addition to model assumptions, the result may also be affected by observational and data reduction uncertainties. Therefore it is important to adopt a statistical approach and use a large sample of H II regions covering a wide range of metallicities to make more definite conclusions on the temperature differences between the O $^{2+}$ and H $^+$ zones.

2.3. Goodness of fit

To judge the goodness of each model's fit to the observed SED, we have computed a mean deviation σ between the observed and modeled spectra for each Monte Carlo realization. To obtain σ , we calculate the root mean square deviations σ_j for each of five continuum regions chosen to cover the whole wavelength range and selected to be devoid of line emission in each spectrum. Two of the selected regions are chosen to be on either side of the Balmer jump and another two on either side of the Paschen jump. They are chosen to be as close as possible to the locations of the two jumps. The five chosen continuum regions are shown by thick horizontal lines in representative MMT and SDSS spectra in Fig. 4, along with the best model fit to the whole spectrum. In the spectra of other objects, the precise location of the continuum regions may vary slightly, depending on the quality of data, the presence of residuals from night sky subtraction, etc. The quantity σ_j is calculated as $\sigma_j = \sqrt{\sum_{i=1}^{N_j} (f_{obs}^i - f_{mod}^i)^2 / N_j}$, where N_j is the number of points in each particular spectral interval. Then $\sigma = \sum \sigma_j / 5$. We did not attempt to fit stellar absorption features such as the hydrogen absorption lines because of their weakness, especially in the lower signal-to-noise ratio SDSS spectra. Additionally, the broad wings of the strong hydrogen emission lines significantly alter the shape of the absorption lines, especially in H II regions with high EW(H β), such as Mrk 71, II Zw 40, SBS 0335–052E and others (see Fig. 1). However, in galaxies with relatively low EW(H β), the hydrogen absorption features are reproduced quite well (see for example the case of I Zw 18 SE in Fig. 2).

To gauge the goodness of the fit, we have used the σ statistic instead of the usual χ^2 test because in the latter statistic, the weight of each region in the overall SED fit depends on the spectrum noise in it. Since the noise is largest in the bluest part of the MMT spectrum which includes the Balmer jump, the weight of this region in the fit is always small. Therefore, the Balmer jump region which plays a crucial role for the determination of $T_e(\text{H}^+)$ is not well fitted by

the model SED if the χ^2 statistic is used. For uniformity, the same σ statistic has been adopted for the SDSS spectra.

In Figure 5 we show the parameter space covered by our Monte Carlo simulations for two BCDs observed with the MMT which are at the extreme ends of the metallicity range of our sample: Mrk 35 which is the highest-metallicity BCD in the MMT sample (upper panel) and SBS 0335–052E which is one of the lowest-metallicity BCDs in it (lower panel). A detailed presentation of the model results for the whole MMT sample will be given in a subsequent paper. There, the star formation history and the stellar populations of each object will be discussed. Calculations have been done for heavy element mass fractions of the stellar populations closest to the heavy element mass fraction of the ionized gas: $Z_{\odot}/2.5$ (Fig. 5a,b) for Mrk 35 and $Z_{\odot}/50$ (Fig. 5c,d) for SBS 0335–052E. In Fig. 5a and 5c, we show only those Monte Carlo realizations that yield a $\text{EW}(\text{H}\beta)$ within $\pm 5\%$ of the observed one, i.e. 2650 out of 10^5 realizations for Mrk 35 and 13972 out of 10^6 realizations for SBS 0335–052E. In those figures, $t_e(\text{H}^+) = T_e(\text{H}^+)/10000$. It is seen that the age $t(\text{old})$ of the old stellar population, the age $t(\text{young})$ of the young stellar population, the ratio b of their masses and the electron temperature $T_e(\text{H}^+)$ in the H^+ zone vary in a wide range. However, if only the 10 best solutions with the lowest σ s are considered, then the range of the electron temperature in the H^+ zone (Fig. 5b and 5d), is considerably narrowed. The adopted temperature is then taken to be the mean of these 10 best temperatures, weighted by σ .

Some other parameters which define the 10 best solutions lie also in a relatively narrow range and their values shown in Fig. 5b and 5d for Mrk 35 and SBS 0335–052E are representative for the whole sample. In particular, $t(\text{young})$ lies in a very narrow range because it depends very sensitively on $\text{EW}(\text{H}\beta)$ and is strongly constrained by it. The ratio b of the masses of old to young stellar populations is typically $\lesssim 10$, corresponding to a luminosity ratio of $\lesssim 10\%$. As for $t(\text{old})$, its range in the 10 best solutions is larger, but is typically between 100 Myr and several Gyr for the whole H II region sample.

We have checked that the derived $t_e(\text{H}^+)$ does not depend sensitively on the exact number of best solutions we choose to average. Fig. 6 shows the mean temperature $t_e(\text{H}^+)$ derived from the 10 best fits vs. the one derived from the 20 best fits for all H II regions in our sample. No systematic deviation from the perfect equality line (dashed line) is seen. We will thus adopt $t_e(\text{H}^+)$ as the weighted mean of the 10 best solutions.

3. Results

3.1. Accuracy of the derived temperatures

Figs. 1 – 3 show by a thick solid line the best fit SED (the one with the smallest σ) superimposed on the redshift- and extinction-corrected observed spectrum of every H II region in the MMT and SDSS samples. In every case, the model SED fits well the observed one over the whole spectral

range, including the Balmer or the Paschen jump region. The separate contributions from the stellar and ionized gas components are shown by thin solid lines. The H II regions are arranged in order of decreasing of $H\beta$ equivalent width, i.e. in order of decreasing contribution of gaseous emission relative to stellar emission. The $t_e(H^+)$ that are derived from the best fits are given in Table 1 for the MMT sample, and in Table 2 for the SDSS sample in the column labeled “inst +inst” (to denote instantaneous bursts for both the young and old stellar populations). We examine next several factors which may affect the electron temperatures so derived.

3.1.1. Differential refraction

We have noted in Sect. 2 that the majority of the H II regions from the MMT sample were observed at parallactic angle. Therefore, differential refraction is not important for those objects. However that was not the case for 3 objects, SBS 0335–052W, SBS 0335–052E and Mrk 71. To check for differential refraction effects in those cases, we have modeled every of the seven individual spectra of SBS 0335–052E obtained at different airmasses. The weighted mean temperature $t_e(H^+)$ of the 10 best SED fits for each observation is plotted as a function of airmass in Fig. 7. There is no evident trend. The absence of dependence of t_e on airmass can probably be explained by the fact that the reddening correction applied to the whole spectrum is based on the observed fluxes of the hydrogen Balmer lines which are themselves subject to differential refraction effects. That procedure thus automatically removes a large part of such effects in the observed SEDs. Therefore we conclude that differential refraction does not significantly affect the electron temperature determination in the three H II regions in our MMT sample that are subject to it. The same conclusion holds for SDSS spectra as well. These were obtained with an airmass not exceeding 1.3.

3.1.2. Continuous star formation

All of our above model fitting was done assuming that the stellar populations contributing to the light of the H II region were formed in two short bursts of star formation, a recent one for the young stellar population, and a prior one for the old stellar population. While the approximation of an instantaneous burst is a good one for the young ionizing stellar population (e.g. Papaderos 1998; Fricke et al. 2001; Noeske et al. 2000), it is probably less so for the old stellar population. The observed SED of the old stellar population in the underlying extended component of a galaxy is more realistically modeled by a continuous star formation, as shown e.g. by Guseva et al. (2001, 2003a,b,c). We wish to investigate how our derived temperatures depend on the adopted star formation history in a galaxy. To this end, we have also carried out Monte Carlo simulations for all objects in the MMT and SDSS samples in which the old stellar population is assumed to be formed not in a short burst, but continuously with a constant star formation rate starting at an initial time t_i and stopping at a final time t_f . This is similar to the approach adopted by Guseva et al. (2001, 2003a,b,c). Since the exact star formation history for the old stellar population is not known, we

choose t_i and t_f to be random numbers between 10 Myr and 15 Gyr with the condition that $t_f \leq t_i$. The best solutions are derived in the same way as for the two burst model simulations. The results of our calculations are shown in Tables 1 and 2 in the column labeled “inst + cont” (to denote that the young stellar population is formed in an instantaneous burst and the old one in a continuous mode). Examination of Fig. 8 where $t_e(\text{inst} + \text{inst})$ is plotted against $t_e(\text{inst} + \text{cont})$ reveals no significant difference between the two temperatures. The relative insensitivity of the derived temperatures $t_e(\text{H}^+)$ to the particular star formation history of the old stellar population is due to the fact that the contribution of this population to the light of the bright H II region is always small, not exceeding a few percent in the optical range. We conclude that the two-burst model is a good approximation to the type of objects considered here. Therefore, in the following, we will consider only results obtained with the two-burst models. They require much less computational time than those with continuous star formation for the old stellar population.

3.1.3. Dependence on the contribution of the gaseous emission and on the oxygen abundance

We show respectively in Figs. 9 and 10 by filled circles the temperature $t_e(\text{H}^+)$ derived from each of the 10 best SED fits for the H II regions in the MMT and SDSS samples. The σ weighted mean of these temperatures is indicated by a straight vertical line in each panel. This mean temperature $t_e(\text{H}^+)$ is listed in Tables 1 and 2 for every H II region, along with the temperature $t_e(\text{O III}) = 10^{-4} T_e(\text{O III})$ derived from the $[\text{O III}] \lambda(4959+5007)/\lambda 4363$ nebular to auroral intensity line ratio. It can be seen from Figs. 9 and 10 that in some cases, Mrk 71A, J0519+0007, HS 0837+4717, HS 0822+3542, SBS 0335–052E and Mrk 35 in Fig. 9, and Mrk 1236, J1402+5416, J1402+5414, J1304–0333, J1228+4407, J1404+5425 and J1403+5421 in Fig. 10, the temperature dispersion is small, corresponding to a relatively deep minimum of σ values in the parameter space and a well-defined $t_e(\text{H}^+)$. In other cases however, the dispersion of the temperatures is larger, corresponding to a broader minimum of σ values and a more uncertain $t_e(\text{H}^+)$.

We wish to examine next which factors may affect the dispersion of $t_e(\text{H}^+)$ and hence limit the precision of its determination. A good measure of that dispersion is the difference between the maximum electron temperature t_{max} and the minimum electron temperature t_{min} of the 10 best solutions. In Fig. 11 we show the dependence of the difference $t_{max} - t_{min}$ on the equivalent width of H β (Fig. 11a), the oxygen abundance $12 + \log(\text{O}/\text{H})$ (Fig. 11b) and the interstellar extinction $C(\text{H}\beta)$ (Fig. 11c) for the whole sample. We find an anti-correlation between $t_{max} - t_{min}$ and EW(H β) with however a large dispersion (Fig. 11a). This implies that, in general, the uncertainty in the $t_e(\text{H}^+)$ determination is smaller for galaxies with a larger contribution of gas emission since the effect of the stellar SED uncertainties is less in these galaxies. A small anti-correlation between $t_{max} - t_{min}$ and the oxygen abundance (Fig. 11b) may be present. This slight trend, if it exists, may be explained by more reliable measurements of the gaseous Balmer or Paschen jumps at higher metallicities. High metallicities lead to lower temperatures of the ionized gas and hence to larger gaseous Balmer and Paschen jumps which can be modeled more accurately. On the other hand,

there is no clear dependence of $t_{max} - t_{min}$ on interstellar extinction (Fig. 11c).

3.2. Comparison of $t_e(\text{H}^+)$ with $t_e(\text{O III})$

We now compare $t_e(\text{H}^+)$ of the H^+ zone derived from the Balmer or Paschen jumps and $t_e(\text{O III})$ of the O^{2+} zone derived from the nebular to auroral line intensity ratio of doubly ionized oxygen $[\text{O III}] \lambda(4959+5007)/\lambda 4363$. In Fig. 12a and 12b, we plot $t_e(\text{H}^+)$ against $t_e(\text{O III})$ for all the objects in our sample respectively for the two-burst and burst+continuous models. The MMT objects are denoted by filled circles and the SDSS objects by open circles. In Fig. 12c and 12d, the same plots are shown but only for objects with relatively deep minima, i.e. those with $\sigma[t_e(\text{H}^+)]/t_e(\text{H}^+) < 10\%$. We have assumed the metallicities of the stars and gas to be the same, an assumption which we relax later. Because of the discreteness in Z of the grid of stellar evolution models, the actual metallicity of the stars may be slightly greater or smaller than the measured ionized gas metallicity. In any case, it is always the one in the grid which is closest to the metallicity of the ionized gas. As before, $t_e(\text{H}^+)$ for each galaxy is the mean of the temperatures derived from the 10 best Monte Carlo realizations weighted by σ . The error bars for $t_e(\text{H}^+)$ show the dispersion from the mean. The solid line denotes equal temperatures while the dashed lines illustrate $\pm 5\%$ deviations from the line of equal temperatures. Examination of Fig. 12 shows there are no systematic differences between the electron temperature $t_e(\text{O III})$ deduced from the collisionally excited $[\text{O III}]$ nebular-to-auroral forbidden line ratio and the temperature $t_e(\text{H}^+)$ derived from the H I recombination spectrum. There are also no systematic differences between the two-burst and the burst+continuous models, either for the whole sample (Figs. 12a and 12b) or for H II regions with deep minima of $t_e(\text{H}^+)$ (Figs. 12c and 12d).

We have also considered the case where the stellar metallicity is less than the ionized gas metallicity. Schaerer et al. (2000) and Guseva et al. (1998) have suggested that there is some hint of a lower metallicity of the stellar population as compared to the metallicity of the ionized gas. To carry out the modeling, we adopt for the metallicity of the stellar population the value of Z in the grid of the stellar evolutionary models which is closest to but lower than the stellar abundance adopted in the $Z_{stars} = Z_{gas}$ case. The results we obtain for the $Z_{stars} < Z_{gas}$ case are very similar to the ones for the $Z_{stars} = Z_{gas}$ case: there are no systematic differences between $t_e(\text{H}^+)$ and $t_e(\text{O III})$.

For comparison, we have also plotted in Fig. 12a data from the literature for H II regions that possess both $t_e(\text{H}^+)$ and $t_e(\text{O III})$ determinations. We have shown by stars in order of increasing $t_e(\text{H}^+)$ the H II regions M16, M20 and NGC 3603 (García-Rojas et al. 2006), the H II region M17 (two data points, Peimbert & Torres-Peimbert 1992), the H II regions the Orion nebula (also two data points, Esteban et al. 1998), the H II regions NGC 3576 (García-Rojas et al. 2004), S 311 (García-Rojas et al. 2005), 30 Dor (Peimbert 2003), NGC 346 (Peimbert et al. 2000) and the two H II regions B and A in the BCD Mrk 71 (González-Delgado et al. 1994). The electron temperatures $t_e(\text{H}^+)$ derived for regions A and B in Mrk 71 by (González-Delgado et al.

1994) using the Paschen jump are some 6000K and 4000K smaller than our values derived from the Balmer jump, leading them to conclude that $t_e(\text{H}^+)$ is smaller than $t_e(\text{O III})$. We find in the contrary that $t_e(\text{H}^+)$ is larger than $t_e(\text{O III})$ for Mrk 71A and equal to $t_e(\text{O III})$ for Mrk 71B. For comparison with the H II region data, we have also plotted in Fig. 12b the data of Liu et al. (2004), Zhang et al. (2004) and Wesson et al. (2005) for 54 Galactic PNe (dots). It is seen that the $t_e(\text{H}^+) - t_e(\text{O III})$ relationship for PNe curves down for objects with $t_e(\text{O III}) \lesssim 1.1$, with $t_e(\text{H}^+)$ being systematically lower than $t_e(\text{O III})$, while the H II region data do not appear to do so except for the lowest-temperature ones. It is not clear why the differences between $t_e(\text{H}^+)$ and $t_e(\text{O III})$ in low-temperature PNe are substantial, while they appear to be less in H II regions in the same temperature range. These differences may be caused by chemical abundance inhomogeneities in PNe as discussed by Liu et al. (2001). If so, these abundance inhomogeneities are absent in the H II regions in both our MMT and SDSS samples.

There is thus no apparent offset of the $T_e(\text{H}^+)$ vs. $T_e(\text{O III})$ relation from the $T_e(\text{H}^+) = T_e(\text{O III})$ line in Fig. 12. For our sample of 47 H II regions, the temperature of the O^{2+} zone is on average equal, within the errors, to the temperature of the H^+ zone. We emphasize that this is a statistical conclusion. Due to the large observational uncertainties for each individual object and those introduced by the assumed star formation history scenario for the modeling of each SED, only a statistical study of a large sample of H II regions can allow us to draw such a conclusion. For hot low-metallicity H II regions, we cannot exclude the presence of small differences of $\sim 3\% - 5\%$ between the temperatures of the O^{2+} zone and H^+ zones, as predicted by Peimbert et al. (2002), since the scatter of the data in Fig. 12 is of that order. In lower temperature H II regions however, we do not observe the larger differences of $\sim 10\%$ predicted by Peimbert et al. (2002). They remain at the level of $\sim 3\% - 5\%$.

It thus appears that the well-known problem of temperature fluctuations raised by Peimbert (1967) affects mainly cool high-metallicity PNe, and to a lesser degree H II regions. As the determination of the primordial He abundance is based mainly on hot low-metallicity H II regions (e.g. Izotov & Thuan 2004), differences between $T_e(\text{H}^+)$ and $T_e(\text{O III})$ of the order of $3\% - 5\%$ should not be a main concern for the derived value of the primordial He abundance. With $T_e(\text{H}^+)$ varying in the range $0.95 - 1 T_e(\text{O III})$, Izotov, Thuan & Stasinska (in preparation, 2006) have shown that the value of the primordial helium abundance would be smaller by $\leq 1\%$ than the value derived assuming $T_e(\text{H}^+) = T_e(\text{O III})$.

4. Conclusions

We have used the Balmer and Paschen jumps to determine the temperatures of the H^+ zones for a total sample of 47 H II regions. The Balmer jump was used on MMT spectrophotometric data of a sample that includes 22 H II regions in 18 blue compact dwarf (BCD) galaxies and one H II region in the spiral galaxy M101. The Paschen jump was used on spectra of 24 H II regions selected from the Data Release 3 of the Sloan Digital Sky Survey. We have employed a Monte

Carlo technique to fit the spectral energy distributions of the galaxies. The main conclusions of the study can be summarized as follows:

1. The electron temperature determination of the H^+ zone by fitting SEDs is more reliable for the galaxies with a larger contribution of the gas emission, i.e. for those with larger $EW(H\beta)$.
2. We find that, for our sample of H II regions, the temperature of the O^{2+} zone determined from the nebular to auroral line intensity ratio of doubly ionized oxygen $[O\ III] \lambda(4959+5007)/\lambda 4363$ is, within the scatter of the data, equal to the temperature of the H^+ zone determined from fitting the Balmer jump and the SED. We cannot however rule out small temperature differences of the order 3–5%.

The MMT time was available thanks to a grant from the Frank Levinson Fund of the Peninsula Community Foundation to the Astronomy Department of the University of Virginia. Y.I.I. and T.X.T. have been partially supported by NSF grant AST-02-05785. The research described in this paper was made possible in part by Award No. UP1-2551-KV-03 of the US Civilian Research & Development Foundation for the Independent States of the Former Soviet Union (CRDF). N.G.G. and Y.I.I. are grateful for the hospitality of the Astronomy Department of the University of Virginia. T.X.T. thanks the hospitality of the Main Astronomical Observatory in Kiev, of the Institut d’Astrophysique in Paris and of the Service d’Astrophysique at Saclay during his sabbatical leave. He is grateful for a Sesquicentennial Fellowship from the University of Virginia. All the authors acknowledge the work of the Sloan Digital Sky Survey (SDSS) team. Funding for the SDSS has been provided by the Alfred P. Sloan Foundation, the Participating Institutions, the National Aeronautics and Space Administration, the National Science Foundation, the U.S. Department of Energy, the Japanese Monbukagakusho, and the Max Planck Society. The SDSS Web site is <http://www.sdss.org/>. The SDSS is managed by the Astrophysical Research Consortium (ARC) for the Participating Institutions. The Participating Institutions are The University of Chicago, Fermilab, the Institute for Advanced Study, the Japan Participation Group, The Johns Hopkins University, the Korean Scientist Group, Los Alamos National Laboratory, the Max-Planck-Institute for Astronomy (MPIA), the Max-Planck-Institute for Astrophysics (MPA), New Mexico State University, University of Pittsburgh, University of Portsmouth, Princeton University, the United States Naval Observatory, and the University of Washington.

REFERENCES

- Aller, L. H. 1984, *Physics of Thermal Gaseous Nebulae*, Dordrecht: Reidel
- Esteban, C., Peimbert, M., Torres-Peimbert, S., & Escalante, V. 1998, *MNRAS*, 295, 301
- Fioc, M., & Rocca-Volmerange, B. 1997, *A&A*, 326, 950
- Fricke, K. J., Izotov, Y. I., Papaderos, P., Guseva, N. G., & Thuan, T. H. 2001, *AJ*, 121, 169

- García-Rojas, J., Esteban, C., Peimbert, M., Rodríguez, M., Ruiz, M. T., & Peimbert, A. 2004, *ApJS*, 153, 501
- García-Rojas, J., Esteban, C., Peimbert, A., Peimbert, M., Rodríguez, M., & Ruiz, M. T. 2005, *MNRAS*, 362, 301
- García-Rojas, J., Esteban, C., Peimbert, M., Costado, M. T., Rodríguez, M., Peimbert, A., & Ruiz, M. T. 2006, *MNRAS*, in press; preprint astro-ph/0601595
- Girardi, L., Bressan, A., Bertelli, G., & Chiosi, C. 2000, *A&AS*, 141, 371
- González-Delgado, R. M., Pérez, E., Tenorio-Tagle, G., et al. 1994, *ApJ*, 437, 239
- Guseva, N. G., Izotov, Y. I., & Thuan, T. X. 1998, *Kinematics and Physics of Celestial Bodies*, 14, 1
- Guseva, N. G., Izotov, Y. I., Papaderos, P., Chaffee, F. H., Foltz, C. B., Green, R. F., Thuan, T. H., Fricke, K. J., & Noeske K. G. 2001, *A&A*, 378, 756
- Guseva, N. G., Papaderos, P., Izotov, Y. I., Green, R. F., Fricke, K. J., Thuan, T. H., & Noeske K. G. 2003a, *A&A*, 407, 75
- Guseva, N. G., Papaderos, P., Izotov, Y. I., Green, R. F., Fricke, K. J., Thuan, T. H., & Noeske K. G. 2003b, *A&A*, 407, 91
- Guseva, N. G., Papaderos, P., Izotov, Y. I., Green, R. F., Fricke, K. J., Thuan, T. H., & Noeske K. G. 2003c, *A&A*, 407, 105
- Izotov, Y. I., & Thuan, T. X. 1998, *ApJ*, 500, 188
- Izotov, Y. I., & Thuan, T. X. 2004, *ApJ*, 602, 200
- Izotov, Y. I., Thuan, T. X., & Lipovetsky, V. A. 1994, *ApJ*, 435, 647
- Izotov, Y. I., Thuan, T. X., & Lipovetsky, V. A. 1997, *ApJS*, 108, 1
- Izotov, Y. I., Stasińska, G., Meynet, G., Guseva, N. G., & Thuan, T. X. 2006, *A&A*, in press; preprint astro-ph/0511644
- Lejeune, T., & Schaerer, D. 2001, *A&A*, 366, 568
- Liu, X.-W., Storey, P.J., Barlow, M.J., Danziger, I.J., Cohen, M., & Bryce, M. 2000, *MNRAS*, 312, 585
- Liu, X.-W., Luo, S.-G., Barlow, M. J., Danziger, I. J., & Storey, P. J. 2001, *MNRAS*, 327, 141
- Liu, Y., Liu, X.-W., Luo, S.-G., & Barlow, M.J. 2004, *MNRAS*, 353, 1231
- Luo, S.-G., Barlow, M.J., Danziger, I.J., & Storey, P.J. 2001, *MNRAS*, 327, 141

- Luridiana, V., Peimbert, A., Peimbert, M., & Cerviño, M. 2003, *ApJ*, 592, 846
- Noeske, K. G., Guseva, N. G., Fricke, K. J., Izotov, Y. I., Papaderos, P., & Thuan, T. H. 2000, *A&A*, 361, 33
- O’Dell, C.R., Peimbert, M., & Peimbert, A. 2003, *AJ*, 125, 2590
- Olive, K. A., & Skillman, E. D. 2004, *ApJ*, 617, 29
- Olive, K. A., Steigman, G., & Skillman, E. D. 1997, *ApJ*, 483, 788
- Papaderos, P., Izotov, Y. I., Fricke, K. J., Guseva, N. G., & Thuan, T. H. 1998, *A&A*, 338, 43
- Peimbert, A. 2003, *ApJ*, 584, 735
- Peimbert, A., Peimbert, M., & Luridiana, V. 2002, *ApJ*, 565, 668
- Peimbert, M. 1967, *ApJ*, 150, 825
- Peimbert, M., & Torres-Peimbert, S. 1992, *Rev. Mexicana Astron. Astrofis.*, 24, 155
- Peimbert, M., Storey, P.J., & Torres-Peimbert, S. 1993, *ApJ*, 414, 626
- Peimbert, M., Peimbert, A., & Ruiz, M. T. 2000, *ApJ*, 541, 688
- Peimbert, M., Peimbert, A., Ruiz, M. T., & Esteban, C. 2004, *ApJS*, 150, 431
- Ruiz, M. T., Peimbert, A., Peimbert, M., & Esteban, C. 2003, *ApJ*, 595, 247
- Schaerer, D., Guseva, N. G., Izotov, Y. I., & Thuan, T. X. 2000, *A&A*, 362, 53
- Thuan, T. X., & Izotov, Y. I. 2005, *ApJS*, 161, 240
- Viegas, S.M., & Clegg, E.S. 1994, *MNRAS*, 271, 993
- Wesson, R., Liu, X.-W., & Barlow, M. J. 2005, *MNRAS*, 362, 424
- Zhang, Y., Liu, X.-W., Wesson, R., Storey, P. J., Liu, Y., & Danziger, I. J. 2004, *MNRAS*, 351, 935
- Zhang, Y., Liu, X.-W., Liu, Y., & Rubin, R. H. 2005a, *MNRAS*, 358, 457
- Zhang, Y., Rubin, R. H., Liu, X.-W. 2005b, *Rev. Mexicana Astron. Astrofis. (SC)*, 23, 15

Table 1. Comparison of $t_e(\text{O III})^a$ and $t_e(\text{H}^+)^b$ for the sample galaxies observed with the MMT.

Galaxy	EW(H β) ^c	$t_e(\text{O III})$	$t_e(\text{H}^+)$		12 + log(O/H)	$C(\text{H}\beta)_{gas}^c$
			inst+inst	inst+cont		
Mrk 71A	397	1.57±0.01	1.87±0.01	1.85±0.03	7.87	0.16
Mrk 94	296	1.27±0.01	1.33±0.12	1.34±0.14	8.11	0.10
II Zw 40	258	1.30±0.01	1.48±0.21	1.39±0.16	8.13	0.96
J 0519+0007	235	1.92±0.02	1.96±0.04	1.98±0.05	7.47	0.13
HS 0837+4717	235	1.91±0.02	1.95±0.06	2.03±0.22	7.60	0.16
HS 0822+3542	232	1.82±0.02	1.94±0.05	1.91±0.09	7.46	0.00
J 1404+5423	228	1.34±0.01	1.41±0.16	1.47±0.13	8.06	0.08
Mrk 209	212	1.56±0.01	1.65±0.29	1.58±0.17	7.82	0.09
SBS 0940+544	207	1.90±0.03	1.85±0.24	1.89±0.30	7.48	0.20
SBS 0335-052E	190	2.00±0.02	1.97±0.05	1.80±0.11	7.31	0.14
Mrk 71B	181	1.47±0.01	1.46±0.16	1.48±0.17	7.91	0.20
SBS 1152+579	169	1.54±0.02	1.67±0.25	1.56±0.08	7.89	0.18
Mrk 35	145	1.01±0.01	1.09±0.08	1.08±0.08	8.34	0.14
Mrk 71C	127	1.39±0.02	1.39±0.16	1.47±0.17	7.91	0.19
Mrk 59(#1)	125	1.35±0.01	1.37±0.26	1.37±0.12	8.01	0.02
I Zw 18SE	124	1.81±0.03	1.82±0.28	1.76±0.22	7.22	0.24
SBS 0926+606A	116	1.31±0.01	1.53±0.12	1.32±0.15	8.01	0.08
SBS 0911+472	98	1.28±0.01	1.31±0.16	1.34±0.15	8.09	0.20
SBS 1030+583	83	1.54±0.02	1.35±0.20	1.58±0.13	7.81	0.04
I Zw 18NW	81	2.00±0.03	1.99±0.38	1.94±0.20	7.17	0.06
SBS 0335-052W	80	1.98±0.13	1.74±0.21	1.90±0.18	7.11	0.12
Mrk 178(#1)	27	1.47±0.03	1.44±0.19	1.51±0.17	7.93	0.04
Mrk 59(#2)	18	1.38±0.03	1.41±0.19	1.33±0.13	8.03	0.00

^a $t_e(\text{O III}) = T_e(\text{O III})/10000$ K, derived from the [O III] $\lambda(4959+5007)/\lambda4363$ emission line ratio.

^b $t_e(\text{H}^+) = T_e(\text{H}^+)/10000$, derived as the weighted mean temperature from the 10 best fits of the SED.

^cEquivalent widths of the H β emission line, oxygen abundances and extinction coefficients derived from the observed Balmer decrement are taken from Thuan & Izotov (2005).

Table 2. Comparison of $t_e(\text{O III})^a$ and $t_e(\text{H}^+)^b$ for the SDSS galaxies.

Galaxy	EW(H β) ^c	$t_e(\text{O III})$	$t_e(\text{H}^+)$		12 + log(O/H)	$C(\text{H}\beta)_{gas}^c$	SDSS spectrum
			inst+inst	inst+cont			
Mrk 94	310	1.29±0.02	1.29±0.11	1.33±0.17	8.07	0.17	0445-51873-404
Mrk 1236	292	1.24±0.02	1.27±0.06	1.36±0.10	8.12	0.14	0481-51908-289
J1402+5416	288	0.91±0.03	0.93±0.05	0.96±0.07	8.53	0.17	1323-52797-008
J1404+5423	284	1.34±0.02	1.60±0.09	1.59±0.08	8.06	0.01	1325-52762-353
J1044+0353	281	1.94±0.06	1.84±0.16	1.82±0.13	7.46	0.06	0578-52339-060
CGCG 007-025	262	1.55±0.03	1.56±0.14	1.43±0.21	7.84	0.00	0266-51630-100
HS 1734+5704	257	1.25±0.02	1.19±0.20	1.38±0.19	8.10	0.03	0358-51818-504
J1403+5422	249	0.97±0.03	1.00±0.10	0.99±0.11	8.48	0.08	1325-52762-352
J0248-0817	246	1.37±0.03	1.47±0.25	1.39±0.25	7.98	0.14	0456-51910-076
J1402+5414	246	0.94±0.02	0.96±0.03	0.95±0.09	8.51	0.16	1323-52797-002
J1253-0312	231	1.35±0.02	1.24±0.20	1.10±0.20	8.04	0.08	0337-51997-097
HS 0837+4717	217	1.92±0.05	1.75±0.16	1.71±0.26	7.60	0.32	0550-51959-092
J1304-0333	201	1.10±0.04	1.00±0.02	1.01±0.03	8.15	0.50	0339-51692-083
J1228+4407	193	0.95±0.02	0.91±0.06	1.04±0.07	8.47	0.26	1371-52821-059
Mrk 1318	169	1.01±0.04	1.05±0.12	1.05±0.17	8.35	0.53	0844-52378-041
J1404+5425	163	1.10±0.03	0.93±0.05	0.92±0.11	8.46	0.08	1325-52762-350
I Zw 18SE	147	1.72±0.07	1.66±0.42	1.78±0.41	7.25	0.10	0556-51991-312
J1403+5421	138	0.86±0.13	0.80±0.08	0.74±0.11	8.17	0.29	1325-52762-345
J1403+5418	128	0.93±0.17	0.77±0.10	0.80±0.11	8.24	0.30	1325-52762-356
J1624-0022	108	1.17±0.03	1.11±0.21	1.24±0.18	8.20	0.10	0364-52000-187
CGCG 032-017	108	1.40±0.03	1.31±0.15	1.40±0.23	8.08	0.40	1185-52642-123
SBS 1222+614	93	1.38±0.03	1.38±0.25	1.35±0.27	8.00	0.04	0955-52409-608
J1038+5330	93	0.98±0.03	0.95±0.14	0.92±0.16	8.37	0.14	1010-52649-328
J1205+5032	72	0.84±0.28	0.88±0.13	0.84±0.19	8.25	0.62	0969-52442-489

^a $t_e(\text{O III}) = T_e(\text{O III})/10000$ K, derived from the [O III] $\lambda(4959+5007)/\lambda4363$ emission line ratio.

^b $t_e(\text{H}^+) = T_e(\text{H}^+)/10000$, derived as the weighted mean temperature from the 10 best fits of the SED.

^cEquivalent widths of the $\text{H}\beta$ emission line, oxygen abundances and extinction coefficients derived from the observed Balmer decrement are taken from Izotov et al. (2006).

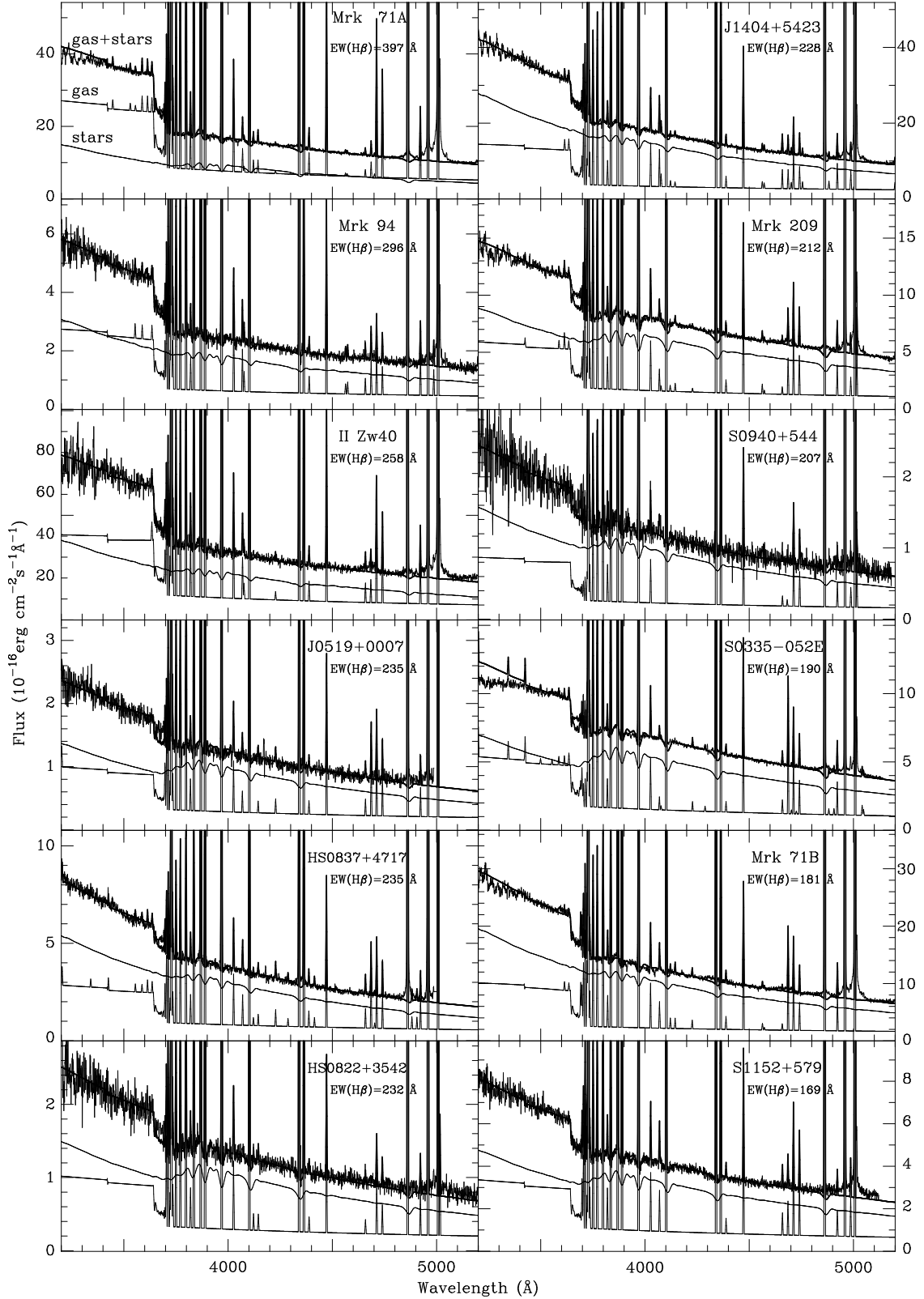


Fig. 1.— Best fit model SEDs (thick solid lines) superposed by the redshift- and extinction-corrected MMT spectra of 22 H II regions in 18 blue compact dwarf galaxies and in one H II region J1404+5423 of the spiral galaxy M101. The separate contributions from the stellar and ionized gas components are shown by thin solid lines (see the labels in the upper left panel for Mrk 71A).

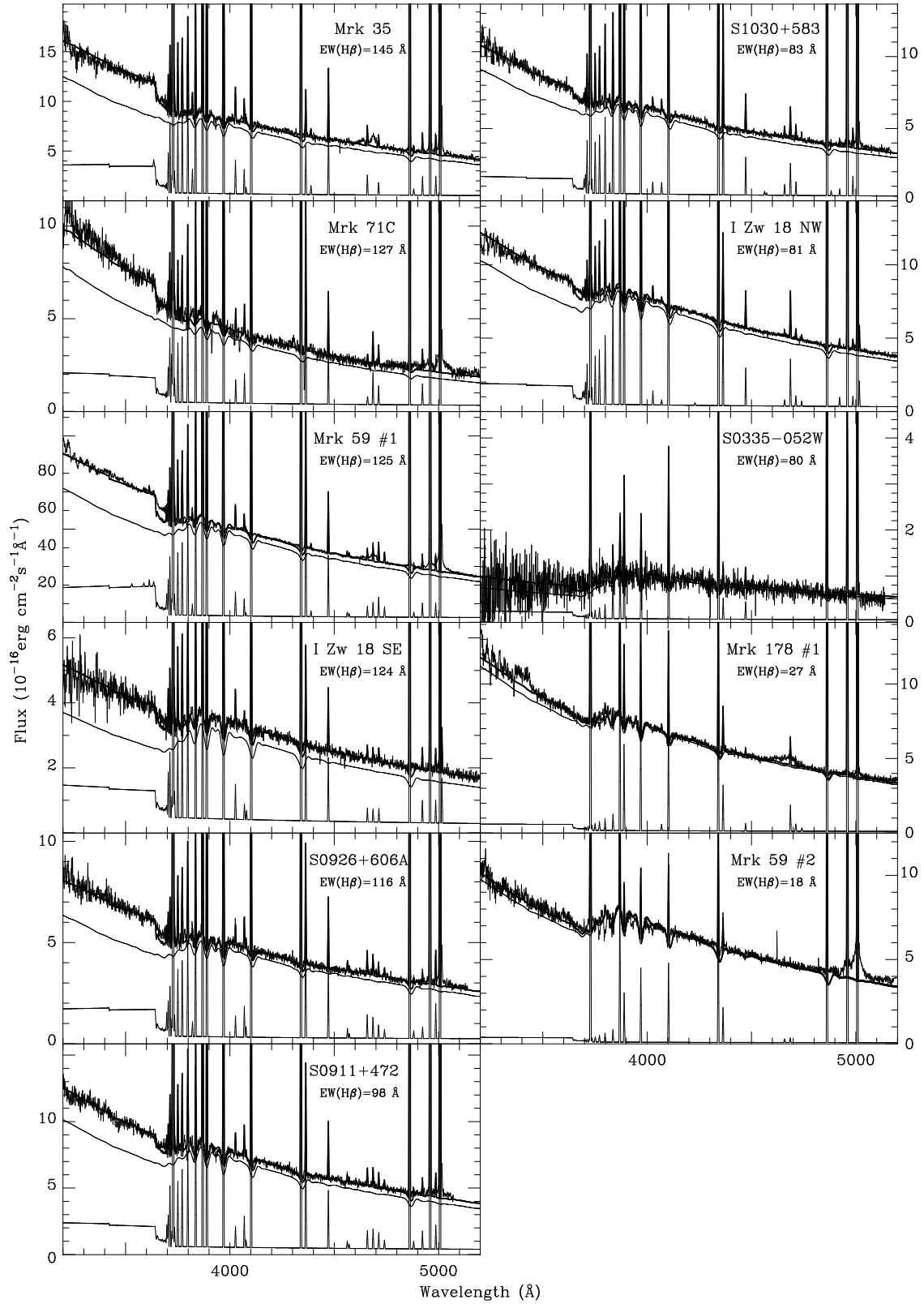


Fig. 1.— Continued.

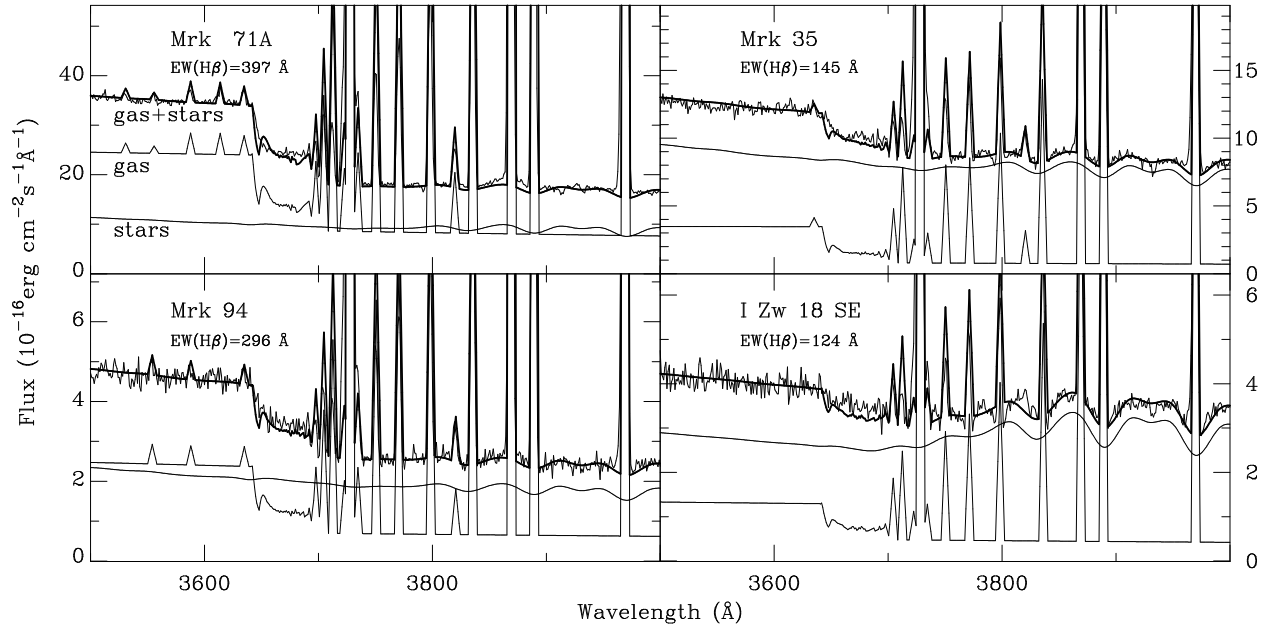


Fig. 2.— Blow-up of the Balmer jump region in 4 selected spectra of Fig. 1.

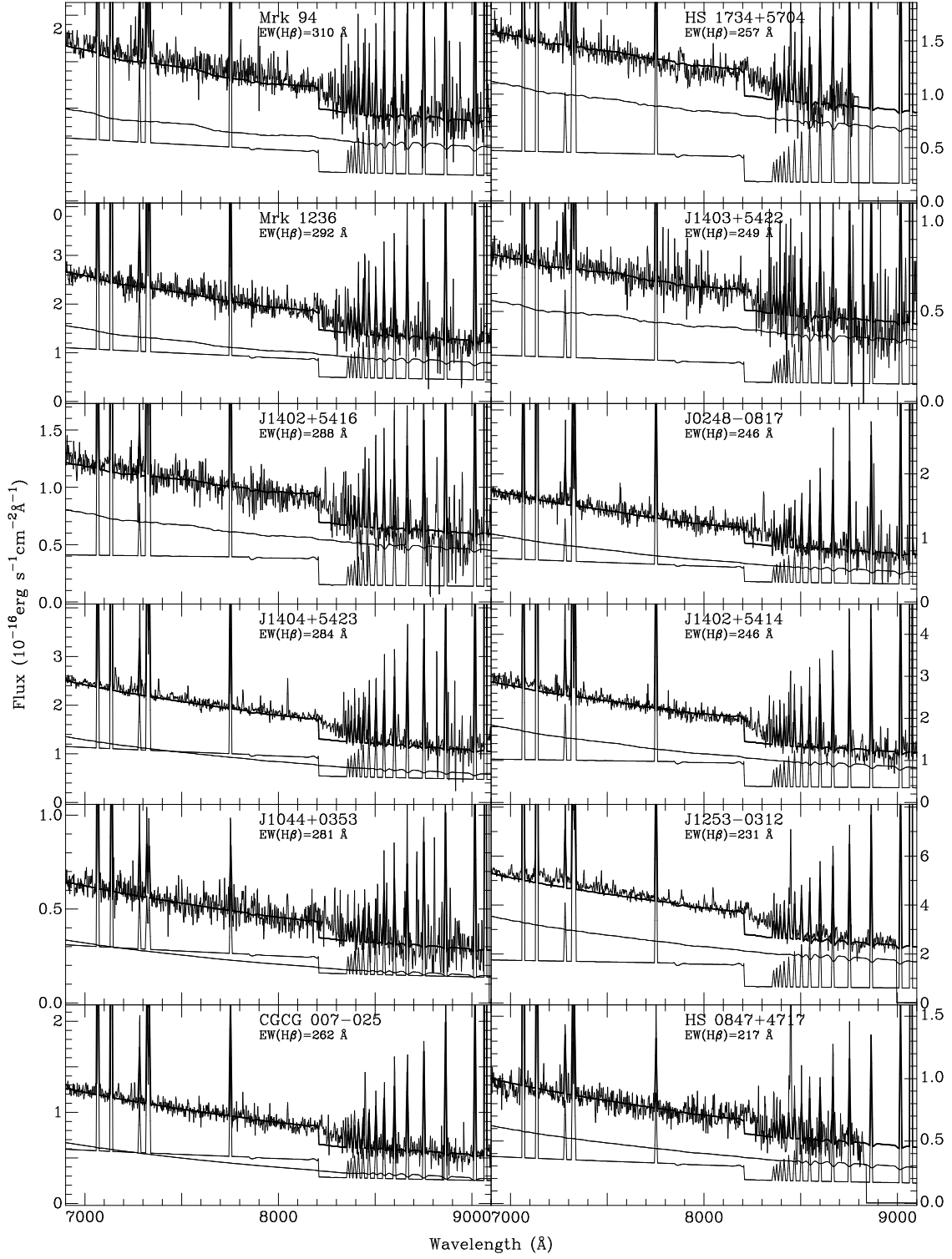


Fig. 3.— Best fit model SEDs (thick solid lines) superposed on the red parts of the redshift- and extinction-corrected SDSS spectra of 11 H II regions in blue compact dwarf galaxies and of 13 H II regions in spiral galaxies. The separate contributions from the stellar and ionized gas components are shown by thin solid lines.

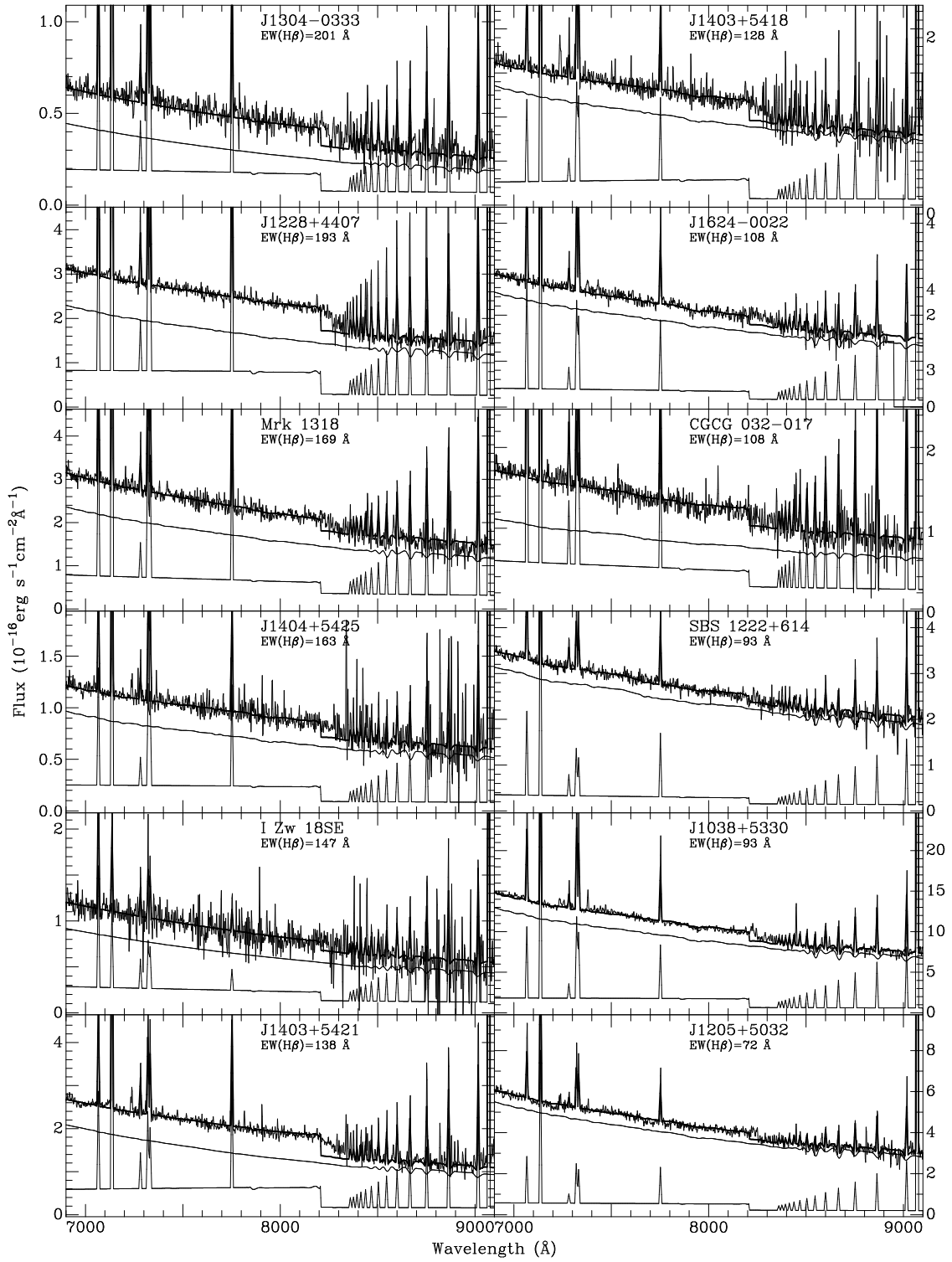


Fig. 3.— Continued.

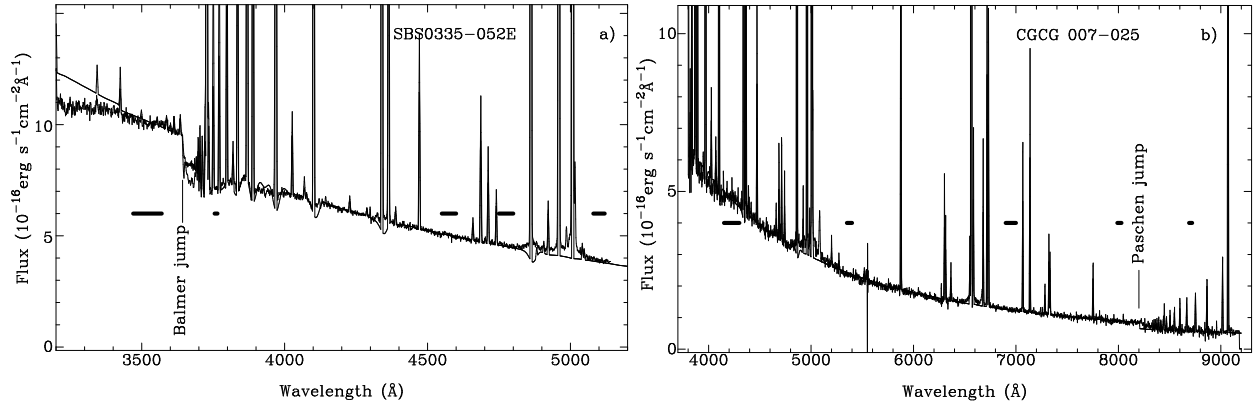


Fig. 4.— Best fit model SED (thick solid lines) superposed on the redshift- and extinction-corrected spectra of SBS 0335-052E (a) and CGCG 007-025 (b). Locations of the Balmer jump in (a) and of the Paschen jump in (b) are marked by vertical lines. The five selected continuum regions used for fitting the observed spectrum are shown by thick horizontal lines in each panel.

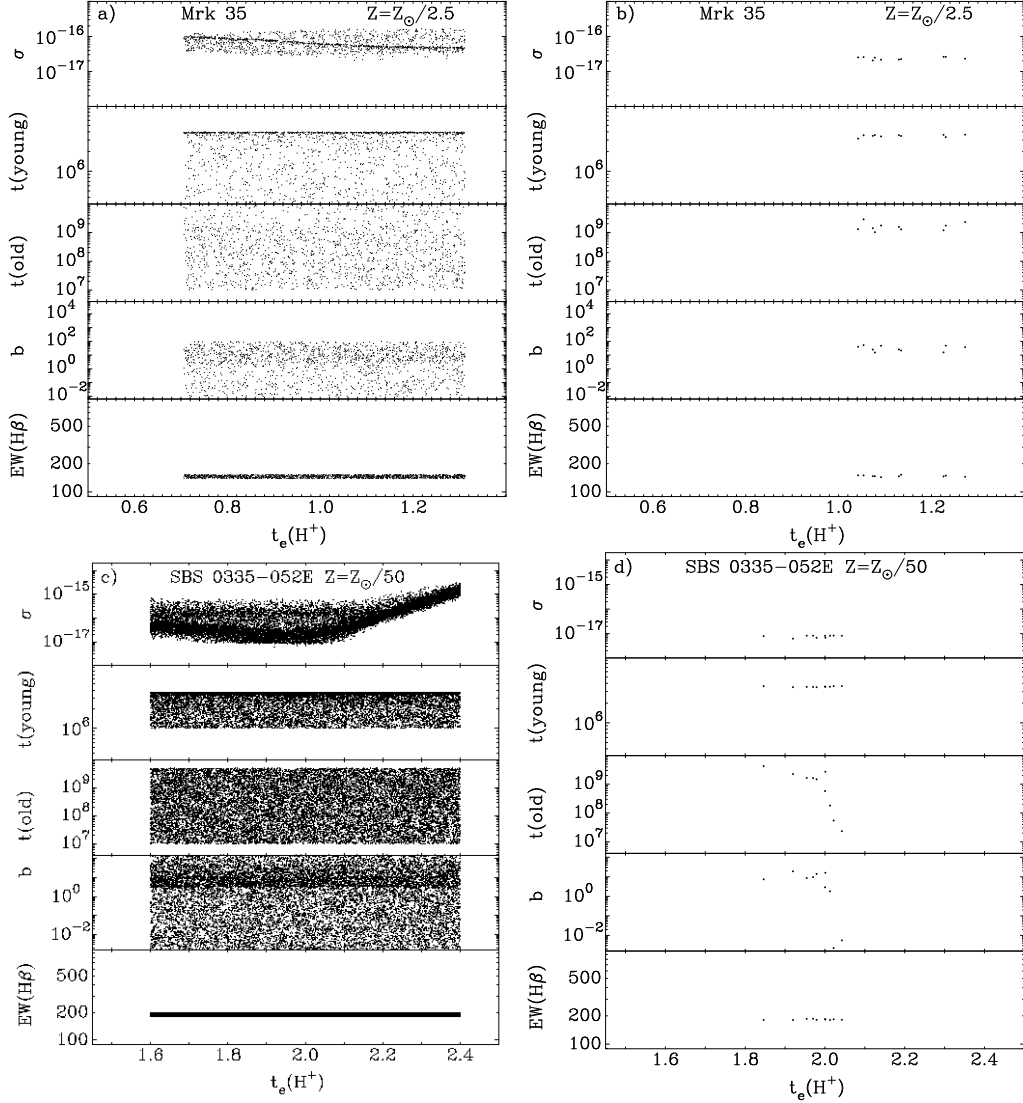


Fig. 5.— Parameter space explored in Monte Carlo simulations to fit the spectra of two BCDs: one is Mrk 35 (panel a), the highest-metallicity BCD in our sample and the other is SBS 0335–052E (panel c), one of the lowest-metallicity BCD in the sample. The parameters shown are: the equivalent width $\text{EW}(\text{H}\beta)$, the ages of the old and young stellar populations, $t(\text{old})$ and $t(\text{young})$, the mass ratio b of the old-to-young stellar populations, and the electron temperature $t_e(\text{H}^+)$ in the H^+ zone. σ is an estimator of the goodness of the fit. Panels (b) and (d) are the same as panels (a) and (c) except that only the 10 best Monte Carlo realizations are shown.

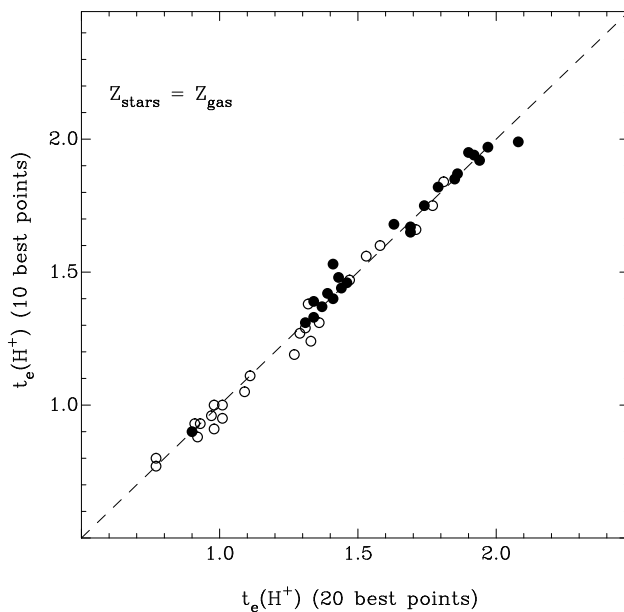


Fig. 6.— The weighted mean temperature $t_e(\text{H}^+)$ of the 10 best SED fits among all Monte Carlo realizations vs. the weighted mean $t_e(\text{H}^+)$ of the 20 best SED fits among all Monte Carlo realizations for each BCD. Equality is shown by a dashed line. H II regions observed with the MMT are shown by filled circles and those from the SDSS by open circles.

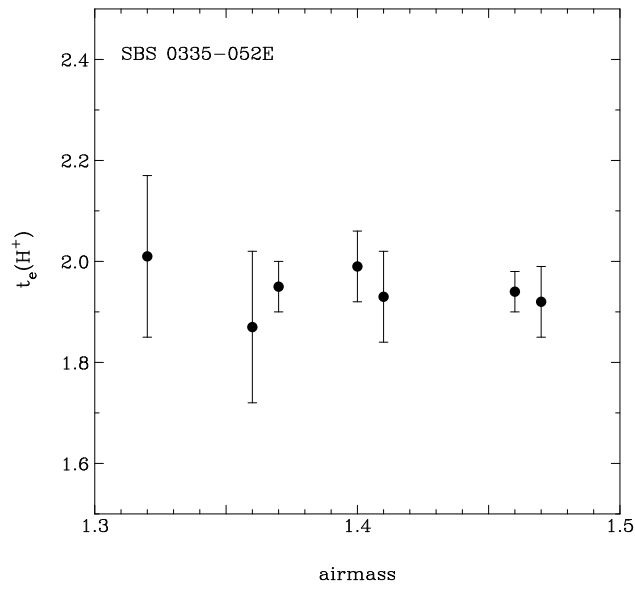


Fig. 7.— The weighted mean temperature $t_e(\text{H}^+)$ derived from different spectra of SBS 0335-052E as a function of airmass.

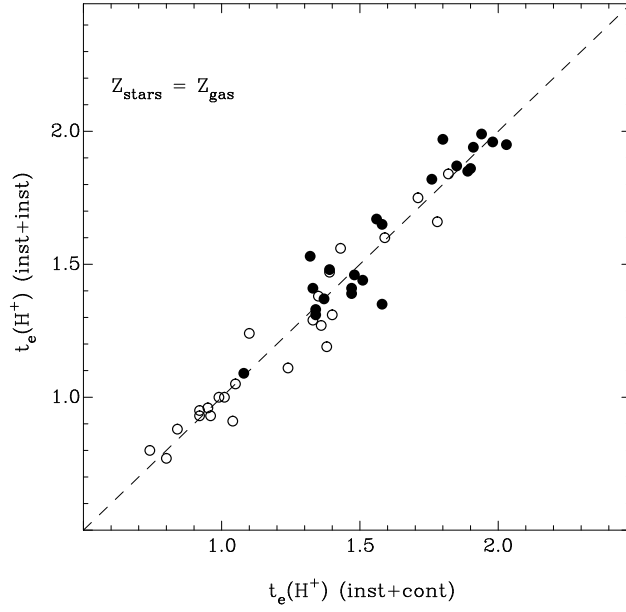


Fig. 8.— Dependence of the derived temperatures in the H^+ regions on the star formation history. The quantity $t_e(\text{H}^+) (\text{inst+inst})$ denotes the temperature derived by fitting the galaxy’s spectrum with a two-burst model, one for the young stellar population and one for the old stellar population, while the quantity $t_e(\text{H}^+) (\text{inst+cont})$ denotes the temperature derived by fitting the galaxy’s spectrum with a model where the young stellar population is made in a short burst and the old stellar population in a continuous mode. No systematic difference is seen between the two temperatures.

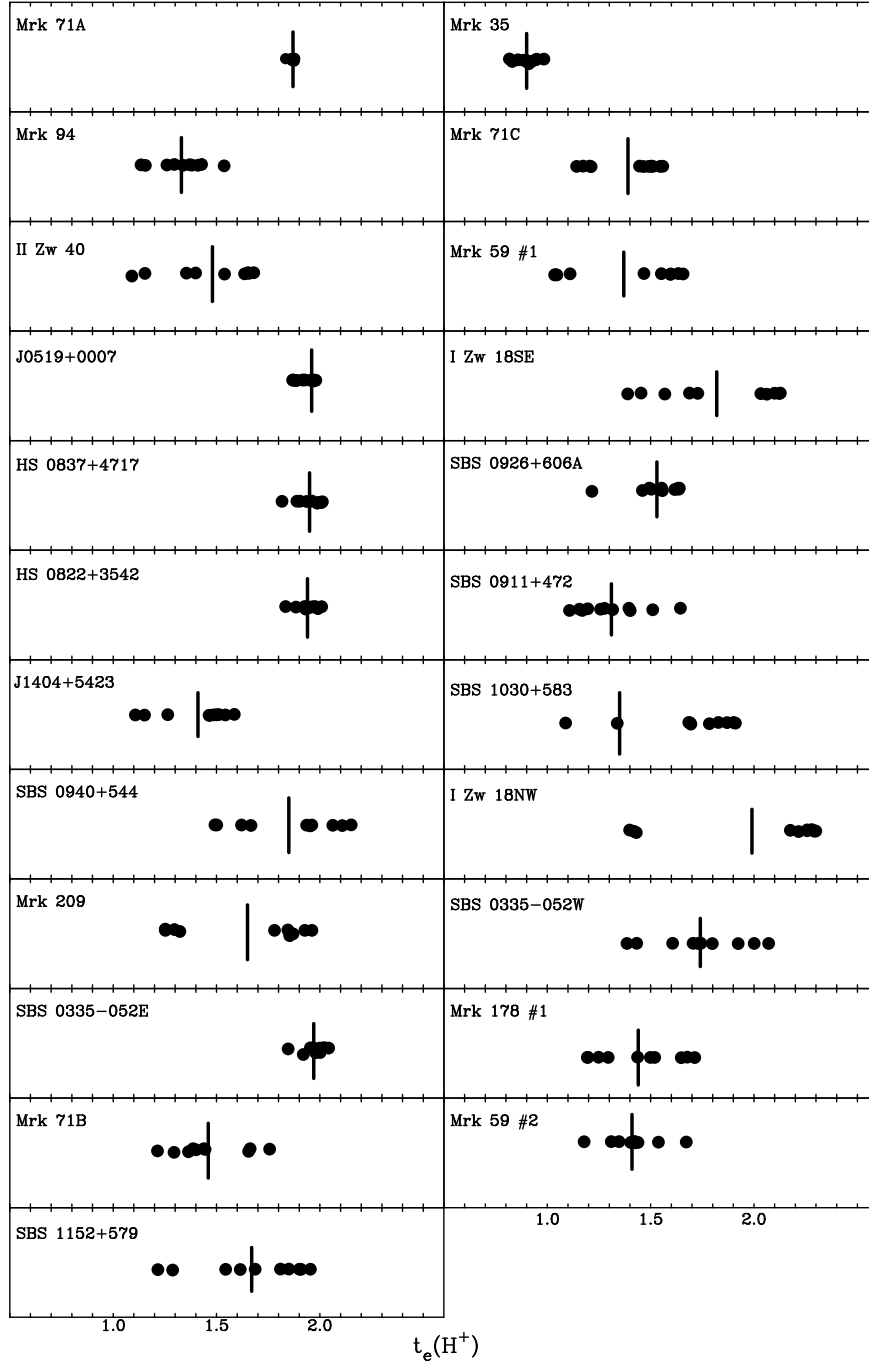


Fig. 9.— Temperature $t_e(\text{H}^+) = 10^{-4} T_e(\text{H}^+)$ of the 10 best SED fits (filled circles) among all Monte Carlo realizations for each H II region observed with the MMT. The mean temperatures weighted by σ are shown by straight vertical lines.

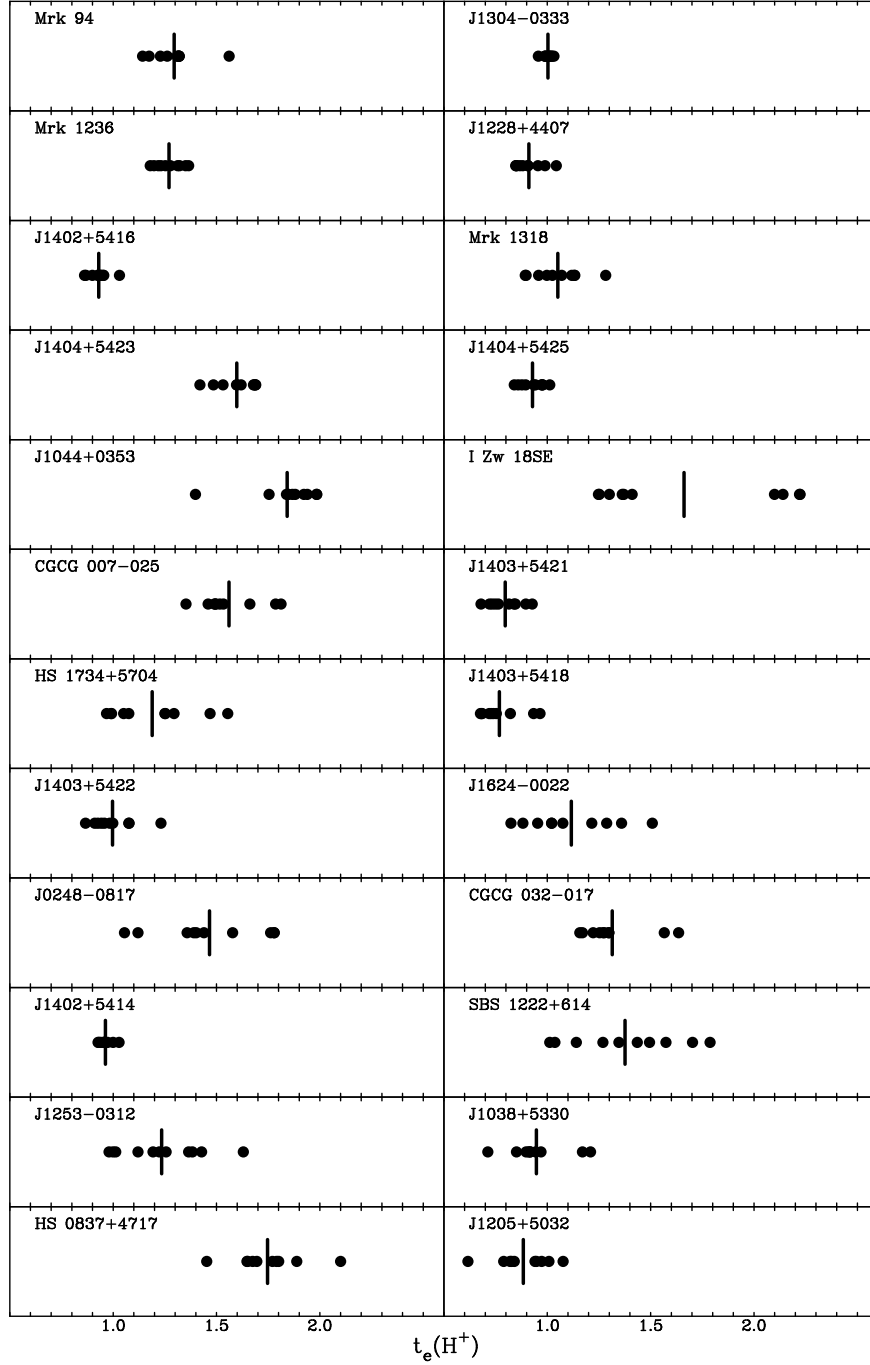


Fig. 10.— Temperature $t_e(\text{H}^+) = 10^{-4}T_e(\text{H}^+)$ of the 10 best SED fits (filled circles) among all Monte Carlo realizations for each H II region extracted from the SDSS. The mean temperatures weighted by σ are shown by straight vertical lines.

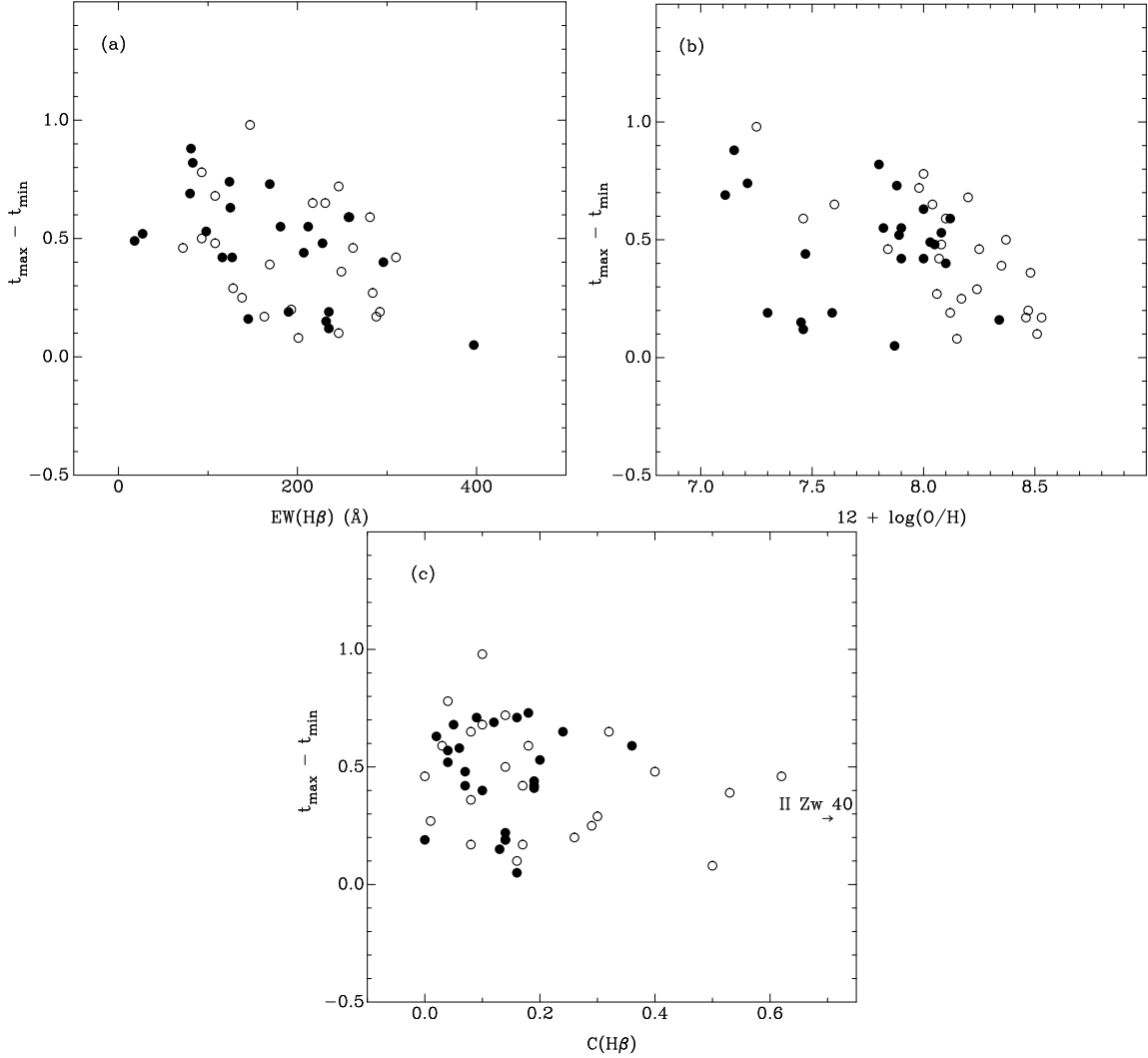


Fig. 11.— Maximal differences ($t_{max} - t_{min}$) of the temperature $t_e(H^+)$ among the 10 best Monte Carlo realizations in each galaxy vs (a) the equivalent width of $H\beta$, (b) the oxygen abundance $12 + \log(O/H)$ and (c) the extinction coefficient $C(H\beta)$. In all panels, the metallicity of the stellar population is set equal to that of the stellar evolutionary model closest to the metallicity of the gas. In panel (c), the extinction of the BCD II Zw 40 is off-scale because it is very nearly in the Galactic plane and is heavily reddened by Galactic extinction. Filled circles show H II regions observed with the MMT, and open circles those from the SDSS.

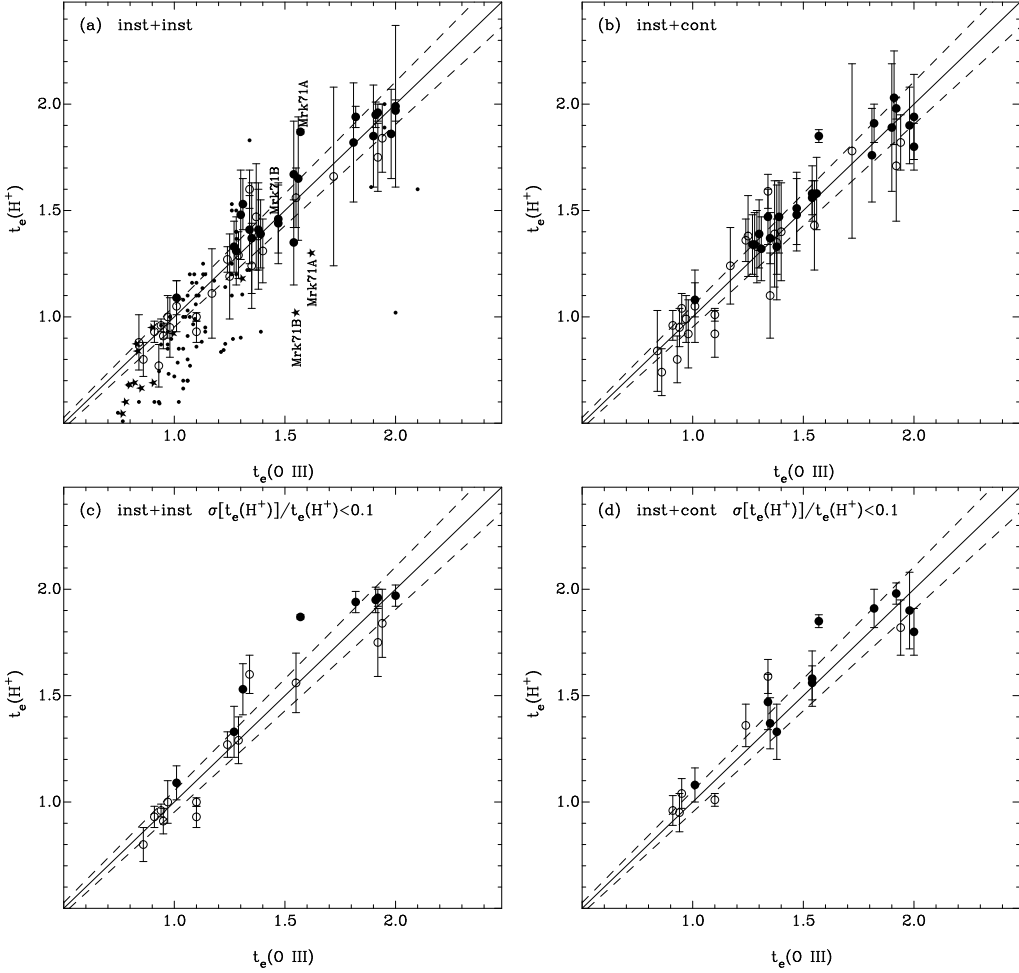


Fig. 12.— Comparison of the temperature $t_e(\text{H}^+)$ derived from fitting the Balmer jump and the SED and of the temperature $t_e(\text{O III})$ derived from the nebular to auroral line intensity ratio of doubly ionized oxygen $[\text{O III}] \lambda(4959+5007)/\lambda 4363$, for all objects in our sample (filled circles show H II regions observed with the MMT and open circles those from the SDSS). Two cases have been considered: (a) the two-burst (inst+inst) model, and (b) the burst+continuous star formation (inst+cont) model. Panels (c) and (d) are the same as panels (a) and (b), but show only H II regions with deep minima for $t_e(\text{H}^+)$. In each panel, the solid line denotes equal temperatures and the dashed lines show a $\pm 5\%$ deviation from the line of equal temperatures. Error bars are the root mean square temperature deviations from the mean of the 10 Monte Carlo simulations. Stars in (a) show the data for H II regions from Esteban et al. (1998), García-Rojas et al. (2004, 2006), Peimbert & Torres-Peimbert (1992), Peimbert et al. (2000), Peimbert (2003) and González-Delgado et al. (1994). For comparison, we have labeled the Mrk 71 A, B data points from the present work and from González-Delgado et al. (1994). Our $t_e(\text{H}^+)$ for Mrk 71 A, B derived using the Balmer jump are considerably higher than those of González-Delgado et al. (1994) using the Paschen jump. For comparison, we have also plotted in (a) the data of Liu et al. (2004), Zhang et al. (2004) and Wesson et al. (2005) for 54 Galactic PNe (dots).